Published in partnership with FCT NOVA with the support of E-MRS



https://doi.org/10.1038/s41699-025-00566-0

## Influence of humidity on the resistive switching of hexagonal boron nitride-based memristors

Check for updates

Lukas Völkel<sup>1</sup>, Rana Walied Ahmad<sup>2</sup>, Alana Bestaeva<sup>2</sup>, Dennis Braun<sup>1</sup>, Sofia Cruces<sup>1</sup>, Jimin Lee<sup>1</sup>, Sergej Pasko<sup>3</sup>, Simonas Krotkus<sup>3</sup>, Michael Heuken<sup>3</sup>, Stephan Menzel<sup>2</sup> & Max C. Lemme<sup>1,4</sup>

Two-dimensional material-based memristors have recently gained attention as components of future neuromorphic computing concepts. However, their surrounding atmosphere can influence their behavior. In this work, we investigate the resistive switching behavior of hexagonal boron nitride-based memristors with active nickel electrodes under vacuum conditions. Our cells exhibit repeatable, bipolar, nonvolatile switching under voltage stress after initial forming, with a switching window >10³ under ambient conditions. However, in a vacuum, the forming is suppressed, and hence, no switching is observed. Compact model simulations can reproduce the set kinetics of our cells under ambient conditions and predict highly suppressed resistive switching in a water-deficient environment, supporting the experimental results. Our findings have important implications for the application of h-BN-based memristors with electrochemically active electrodes, since semiconductor chips are typically processed under high vacuum conditions and encapsulated to protect them from atmospheric influences.

Two-dimensional (2D) materials have attracted attention as the active medium in resistive switching devices<sup>1-3</sup>. Hexagonal boron nitride (h-BN) is of special interest, as it is an atomically thin insulator with a band gap of approximately 6 eV<sup>4</sup>, promising low energy consumption<sup>5</sup>, fast switching<sup>6</sup>, and a large switching window. h-BN has been shown to exhibit both nonvolatile and volatile (threshold) resistive switching behavior<sup>7</sup>. The predominant resistive switching mechanism discussed in the literature is metallic filament formation under voltage stress<sup>8-10</sup>, analogous to electrochemical metallization (ECM) cells based on more mature metal oxides<sup>11</sup>. Ambient air molecules, such as water, can significantly influence the resistive switching behavior of metal oxide-based ECM cells<sup>12</sup>. In the last years, extensive studies have examined the effects of moisture and oxygen on the resistive switching of ECM metal-oxide memristors 12-16. For instance, Tappertzhofen et al.<sup>13</sup> performed cyclic voltammetry (CV) measurements on Cu/SiO<sub>2</sub>/Pt cells in a dry nitrogen atmosphere with varying water partial pressures. The experiments revealed a clear dependence of the ion concentration inside the cells and the diffusion coefficient of the ions on the water partial pressure<sup>13</sup>. Tsuruoka et al. <sup>15</sup> performed CV measurements on Cu/Ta<sub>2</sub>O<sub>5</sub>/Pt ECM cells at different relative humidity levels, demonstrating a clear dependence of the redox peaks in the CV curves on the relative humidity<sup>15</sup>. Lübben et al. <sup>16</sup> investigated the effect of water partial pressure on the forming voltage of Pt/Ta<sub>2</sub>O<sub>5</sub>/Ta and Pt/ HfO<sub>2</sub>/Hf cells<sup>16</sup>. They observed a significant increase in the forming voltage under low water partial pressure, with forming eventually becoming impossible after drying the cells under vacuum conditions. The role of water in the resistive switching of 2D material-based memristors remained unexplored until 2018, when Wang et al.<sup>17</sup> compared the electrical characteristics of Au/Ti/h-BN/Cu devices immediately after fabrication and after two months of exposure to air with 80% relative humidity<sup>17</sup>. They found an increase in the set voltage after two months of air exposure compared to the fresh devices, which they attributed to a dielectric screening effect: water molecules migrate between the h-BN and the top electrode and form a dielectric screening layer. The dielectric screening layer effectively reduces the applied electric field over the h-BN and thus leads to a higher set voltage. Heating reversed this effect, restoring the device to its initial state. This effect is not related to electrochemical processes and is not observed in metal oxide-based cells. Thus, water could play a different or additional role in the resistive switching of h-BN-based memristors compared to metal-oxide memristors. On the other hand, 2D materials are known to be affected by environmental contaminants<sup>18</sup> and, for example, graphene devices can be used as humidity sensors utilizing electrochemical effects<sup>19,20</sup>.

<sup>1</sup>Chair of Electronic Devices, RWTH Aachen University, Aachen, Germany. <sup>2</sup>Jülich Aachen Research Alliance (JARA)-Fit and Peter Grünberg Institute (PGI-7), Forschungszentrum Jülich GmbH, Jülich, Germany. <sup>3</sup>AIXTRON SE, Herzogenrath, Germany. <sup>4</sup>AMO GmbH, Advanced Microelectronic Center Aachen, Aachen, Germany. ⊠e-mail: max.lemme@eld.rwth-aachen.de

Nevertheless, the effect of vacuum, i.e., the absence of water and other air molecules, on the resistive switching behavior of h-BN memristors remains largely unexplored.

Here, we investigate the influence of ambient conditions on nonvolatile h-BN memristors by comparing their resistive switching behavior under ambient air and vacuum environments. We support our experimental findings by simulating the structures in ambient and vacuum-like environments with a JART ECM compact model<sup>21,22</sup>.

#### Results and discussion Device fabrication

For this study, we fabricated vertical memristors with h-BN sandwiched between two metal electrodes. A schematic view of the material stack is depicted in Fig. 1a. The memristors consist of a 50 nm titanium/palladium (Ti/Pd) bottom electrode (BE), h-BN, and a 60 nm nickel/aluminum (Ni/Al) top electrode (TE) on a silicon (Si) chip with 300 nm thermally oxidized silicon dioxide (SiO<sub>2</sub>). More fabrication details can be found in the experimental section. A top-view optical micrograph of a fabricated cross-point device is shown in Fig. 1b. The active area of the devices was ~30  $\mu\text{m}^2$  (Fig. 1b). The thickness of the transferred h-BN was measured via atomic force microscopy (AFM) to be ~3 nm (Fig. 1c). Raman measurements were conducted on top of the transferred film and on the substrate to confirm the presence of h-BN (Fig. 1d). The Raman spectrum exhibits the characteristic h-BN  $E_{2g}$  Raman peak at  $1368~\text{cm}^{-1.23}$ , which is absent when it is measured next to the h-BN film on the same chips.

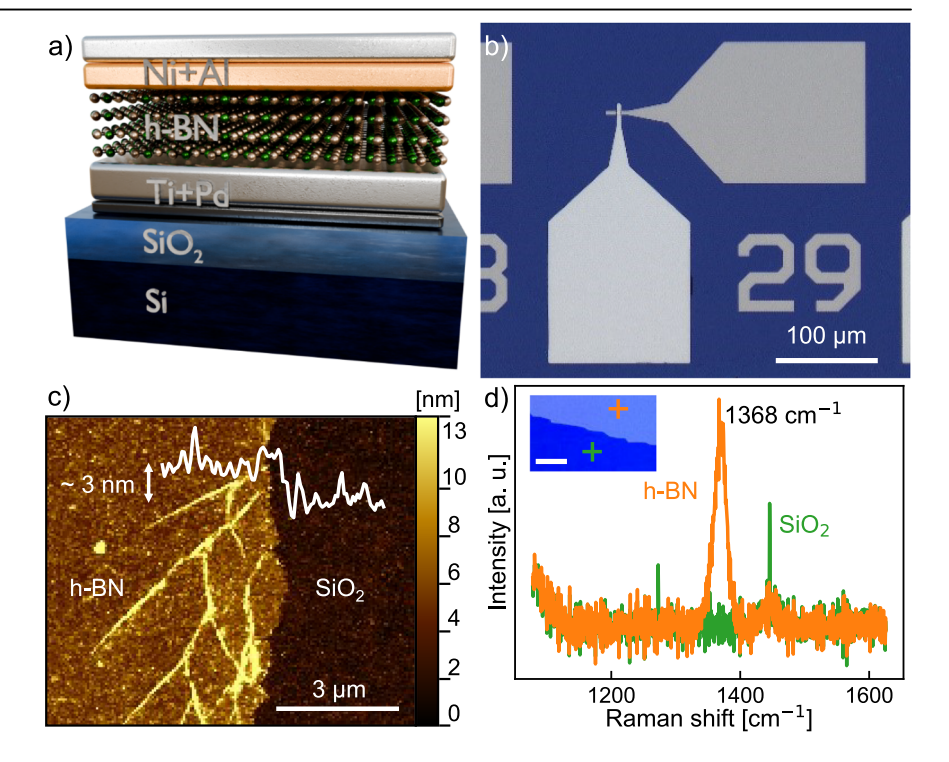
### Direct current electrical characterization and influence of vacuum on the resistive switching behavior

We performed electrical measurements in a cryogenic probe station "CRX-6.5 K" from LakeShore Cryotronics connected to a Tektronix "4200A-SCS" semiconductor parameter analyzer. The voltage was applied to the TE while the BE was grounded. Initially, our devices were in a high resistance state (HRS). We performed DC current-voltage (I-V) measurements by sweeping the voltage from 0 V to 2.5 V and back, and then to -1.4 V and back while measuring the resulting device current. The voltage stress led to repeatable bipolar resistive switching with a set voltage of  $\sim$  1.7 V and a reset voltage of  $\sim$ 

-0.8 V. The sweep rates until the switching events were  $\sim$ 450 mV/s in the positive sweep direction and  $\sim$ 180 mV/s in the negative sweep direction. Figure 2 shows 500 successively measured DC I-V sweeps. The inset shows the low resistance state (LRS) and HRS values over the cycle number with an average resistance window of >10 $^3$ .

We performed DC I-V measurements under vacuum to investigate the influence of ambient air on the resistive switching behavior. The first switching event observed in a pristine memristor under voltage stress is typically called "forming". This term arises from the formation of the first filament in filamentary switching devices, which establishes the foundation for subsequent resistive switching cycles<sup>24</sup>. Figure 3 shows the forming attempts (*I-V* sweeps) of eight devices under both ambient (left) and vacuum (right) conditions each. Vacuum conditions were achieved by pumping down the measurement chamber for 67 h. The pressure during the vacuum measurements was  $4.8 \times 10^{-5}$  mbar. The switching parameters forming voltage  $V_{\text{form}}$  and current  $I_{\text{form}}$  that lead to the successful forming of the devices in ambient air are shaded in gray in both plots. Under ambient conditions, the initial filament was formed for all devices when the applied voltage and the device current exceeded +2.7 V and 20 nA, respectively. In contrast, no initial filament was formed under the same electrical conditions in a vacuum, even after multiple attempts. Further increases in the applied voltage resulted in a forming at higher voltages and currents. However, subsequent reset attempts required high reset voltages that caused permanent breakdown after one or two more voltage sweeps. The I-V curves of three devices formed in vacuum are shown in the Supplementary Fig. 1. Devices initially formed under ambient conditions and subsequently measured in vacuum conditions also did not show stable resistive switching (see Supplementary Fig. 2). We also performed area-dependent measurements of the initial resistance and forming voltage under both ambient and vacuum conditions, which can be found in the Supplementary Fig. 3. The initial resistance decreases with increasing device area because the entire device area contributes to the current conduction. The current, therefore, scales with device area. Consequently, the forming voltage also decreases as the device area increases. Notably, for devices smaller than ~300 μm<sup>2</sup>, the forming voltage in ambient conditions is significantly lower than in vacuum. No such difference is observed for larger devices.

Fig. 1 | Device fabrication. a Schematic of our fabricated Pd/h-BN/Ni memristors on a Si/SiO $_2$  substrate. b Micrograph of a cross-point device. The h-BN covers the entire area below the top electrode. c AFM measurement of h-BN transferred to SiO $_2$ . The white line at the top shows the thickness profile along the edge. The h-BN thickness is ~3 nm. d Comparative Raman measurements of h-BN and SiO $_2$ . The measurement positions are marked in the micrograph (inset). The scale bar is 10  $\mu$ m. The Raman spectrum of the h-BN shows a characteristic peak at 1368 cm $^{-1}$ .



#### Experimental determination of the set kinetics and its simulation

A set kinetics plot describes the relationship between the set time and the applied voltage of a memristor<sup>25</sup>. In ECM cells, this relationship allows insights into the time-limiting processes during the resistive switching event. These processes can be nucleation-limited, redox-based, electron transferlimited, and ion migration-limited<sup>26</sup>. While the change in the applied voltage is small, the set time varies by orders of magnitude. We applied voltage pulses with pulse widths ranging from minutes down to the nanosecond timescale. Figure 4a shows an example of a set pulse with a pulse amplitude of 5 V and a preset pulse width of 10 µs, leading to a switching time of  $t_{\text{set}} = 6.4 \,\mu\text{s}$ . The current limit was set to 50  $\mu\text{A}$  during the measurement. Notably, the real pulse width seems to be shorter (equal to  $t_{set}$ ) than the preset value. This occurs because the current-limiting circuit regulates the output voltage down to ensure a maximum current of 50 µA after the device switches from the HRS to the LRS. In Fig. 4a, the current increases abruptly after 6.4 µs due to the set transition, which leads to a current overshoot but gets limited to 50 µA after ~900 ns by the current-limiting circuit. The voltage pulse ends when the current drops to 0 A. Repeating this experiment for different pulse amplitudes results in a characteristic set kinetics plot (Fig. 4b). All fast voltage pulses (pulse width up to 10 ms) and respective current responses and an exemplary set event after constantly biasing our device with 1.4 V for several hundred seconds can be found in the Supplementary Fig. 4. The relationship between the set time and the applied voltage is well described by a simplification of the Butler-Volmer equation<sup>27,28</sup>, as implemented in the JART ECM model<sup>21,22</sup> and is illustrated by the orange line in Fig. 4b. The model assumes three different contributions to the ionic device current during resistive switching: (1) the current flow from the electron transfer reactions (redox reactions) at the active electrode/h-BN interface  $(I_{ac})$ ; (2) the current flow at the h-BN/filament tip interface  $(I_{fil})$ ; and (3) the

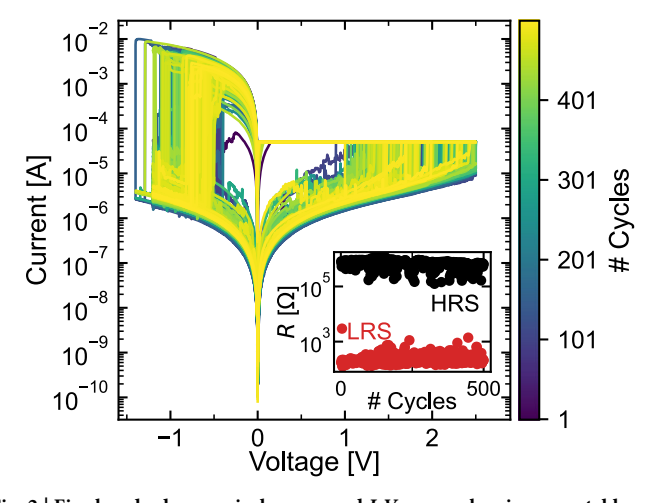


Fig. 2 | Five hundred successively measured I-V curves showing repeatable bipolar resistive switching of one memristor. The inset plot shows the resistances of the high (HRS) and low resistive states (LRS) with an increasing number of cycles.

current flow caused by the ion migration process ( $I_{\text{hop}}$ ). The redox reaction current is described by the Butler-Volmer equation, highlighting the importance of redox reactions during resistive switching:

$$\begin{split} I_{\text{ac/fil}} &= \pm zeck_{0,\text{et}}A_{\text{ac/fil}} \exp\left(-\frac{\Delta G_{\text{et}}}{k_{\text{B}}T}\right) \cdot \left[\exp\left(\frac{\left(1 - \alpha_{\text{et}}\right)ze}{k_{\text{B}}T}\eta_{\text{ac/fil}}\right) - \exp\left(-\frac{\alpha_{\text{et}}ze}{k_{\text{B}}T}\eta_{\text{ac/fil}}\right). \end{split} \tag{1}$$

Here, z is the charge transfer number, e is the elementary charge, c is the nickel ion concentration,  $k_{0,\text{et}}$  is the electron transfer reaction rate,  $A_{\text{ac/fil}}$  are the (circular) active electrode reaction area and the filament area, respectively,  $\Delta G_{\text{et}}$  is the electron transfer activation barrier,  $k_{\text{B}}$  is the Boltzmann constant, T is the temperature,  $\alpha_{\text{et}}$  is the electron transfer coefficient, and  $\eta_{\text{ac/fil}}$  is the respective electron transfer overpotential. The current flow caused by the ion migration process is described by the Mott-Gurney law<sup>29</sup>:

$$I_{hop} = 2zecaf \exp\left(-\frac{\Delta G_{hop}}{k_{\rm B}T}\right) A_{\rm is} \sinh\left(\frac{aze}{2k_{\rm B}T}\frac{\eta_{hop}}{x}\right), \tag{2}$$

where a is the mean ion hopping distance, f is the hopping attempt frequency,  $\Delta G_{\rm hop}$  is the ion hopping activation barrier,  $A_{\rm is}$  is the cross-sectional area of the ion migration in the switching layer,  $\eta_{\rm hop}$  is the ion hopping overpotential and x is the tunneling gap between the tip of the filament and the active electrode. By inserting one of the ionic currents  $I_{\rm ac}$ ,  $I_{\rm fib}$ , or  $I_{\rm hop}$  as the current density  $j_{\rm ion}$  into Eq. 3,

$$\frac{\partial x}{\partial t} = -\frac{M_{\text{Me}}}{ze \, \rho_{\text{m,Me}}} j_{\text{ion}},\tag{3}$$

the transient evolution of the tunneling gap x depending on the ionic current density  $j_{\rm ion}$  is described, and thus, the evolution of the filament. In Eq. 3,  $M_{\rm Me}$  and  $\rho_{\rm m,Me}$  are the molecular mass and mass density of nickel, respectively. The switching time  $t_{\rm set}$  is mainly determined by Eq. (3). All the model parameters are summarized in Table 1, and the full model is presented in refs. 21,22.

We fitted the experimental data by applying Eq. 3 with two different Ni ion concentrations c, as shown in Fig. 4b. The first slope of the simulated curves is determined by the redox-based electron transfer processes. Here, this is the first regime for small or intermediate applied voltages, and the redox processes are the slowest of the ionic processes. The second slope represents a switching time limitation through a combination of redox processes at the interfaces and ionic migration processes through the switching layer. Both ionic processes simultaneously limit the switching speed for high voltages<sup>21,22</sup>. Valov and Tsuruoka extensively studied the electrochemical processes in  $SiO_2$ — and  $Ta_2O_5$ —based ECM cells and concluded that two electrochemical processes are relevant for filament formation during the initial forming of a pristine device and after strong reset events<sup>14</sup>: the anodic oxidation of the active metal electrode at the active

Fig. 3 | Forming attempts of eight devices each under ambient (left) and vacuum (right) conditions. The gray areas indicate the forming voltage and forming current ranges that lead to successful forming under ambient conditions. The parameters used under ambient conditions did not lead to forming under vacuum.

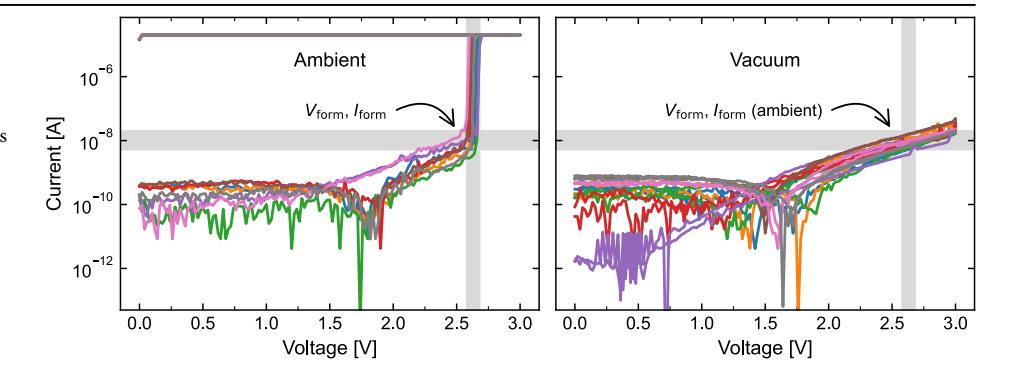


# Fig. 4 | Set pulse current response and resulting set kinetics plot under ambient and vacuum conditions. a Example set pulse and current response with a pulse width of 10 $\mu$ s. The voltage pulse appears to be shorter because the current-limiting circuit decreases the applied voltage after the set event. The current limit was set to 50 $\mu$ A. The gray area indicates the set time $t_{\rm set}$ . b Set kinetics plot with extracted set times $t_{\rm set}$ versus the applied voltage pulse amplitude. The trend of the experimental data under ambient conditions can be described by the Butler-Volmer equation (orange line). A decreased Ni ion concentration c reflects vacuum-like conditions, leading to significantly longer switching times (green line).

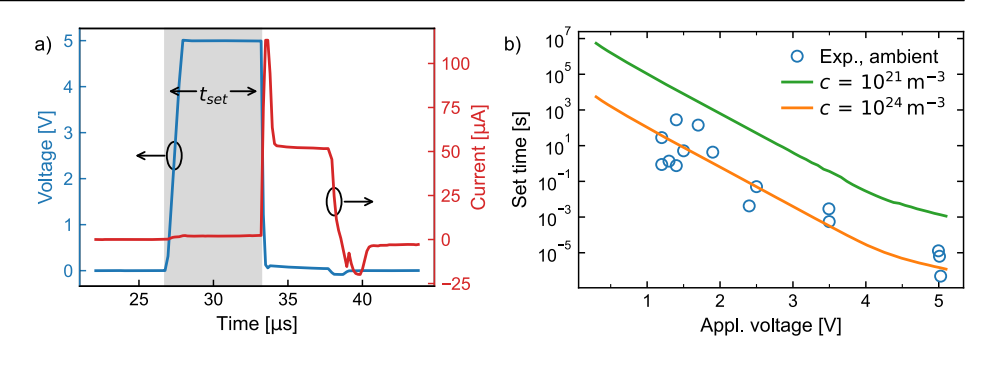


Table 1 | Model parameters, descriptions, and values

Value	Symbol/Parameter	Value
9.75·10 <sup>−26</sup> kg	r <sub>ac</sub> : radius of active electrode reaction area A <sub>ac</sub>	10 nm
2	$r_{ m fil}$ : filament radius of a filament area $A_{ m fil}$	1 nm
8.91·10³ kg/m³	$r_{\rm is}$ : cross-sectional radius of the ion hopping process	10 nm
2.21	L: length of switching/insulating layer	3 nm
3.71 eV	$ ho_{ m fil}$ : filament's electronic resistivity	6.85·10 <sup>−8</sup> Ωm
0.07	R <sub>el</sub> : resistance of electrodes	40 Ω
1·10³ m/s	R <sub>S</sub> : series resistance	120 Ω
1·10 <sup>24</sup> 1/m <sup>3</sup>	T: temperature	298 K
0.65 eV	$t_{0, m nuc}$ : prefactor of nucleation time	6·10 <sup>−10</sup> s
	ΔG <sub>nuc</sub> : nucleation activation energy	0.8 eV
9.11·10 <sup>-31</sup> kg 6.63·10 <sup>-34</sup> J s 1.60·10 <sup>-19</sup> C 1.38·10 <sup>-23</sup> J/K	$N_{\rm c}$ : number of atoms for stable nucleus $a_{\rm nuc}$ : electron transfer coefficient for nucleation a: mean ion hopping distance $f$ : ion hopping attempt frequency $\Delta G_{\rm hop}$ : ion migration barrier	3 0.3 0.17 nm 1·10 <sup>13</sup> Hz 0.22 eV
	9.75·10 <sup>-26</sup> kg  2  8.91·10 <sup>3</sup> kg/m <sup>3</sup> 2.21  3.71 eV  0.07  1·10 <sup>3</sup> m/s  1·10 <sup>24</sup> 1/m <sup>3</sup> 0.65 eV  9.11·10 <sup>-31</sup> kg 6.63·10 <sup>-34</sup> J s 1.60·10 <sup>-19</sup> C	9.75· $10^{-26}$ kg $r_{ac}$ : radius of active electrode reaction area $A_{ac}$ 2 $r_{fil}$ : filament radius of a filament area $A_{fil}$ 8.91· $10^3$ kg/m³ $r_{is}$ : cross-sectional radius of the ion hopping process  2.21 $L$ : length of switching/insulating layer  3.71 eV $\rho_{fil}$ : filament's electronic resistivity  0.07 $R_{el}$ : resistance of electrodes  1· $10^3$ m/s $R_s$ : series resistance  1· $10^2$ 4 1/m³ $T$ : temperature  0.65 eV $t_{0,nuc}$ : prefactor of nucleation time $\Delta G_{nuc}$ : nucleation activation energy  9.11· $10^{-31}$ kg $N_c$ : number of atoms for stable nucleus $n_{nuc}$ : electron transfer coefficient for nucleation

electrode/insulator interface, here

$$Ni \to Ni^{2+} + 2e^-,$$
 (4)

and the reduction reaction at the insulator/inert electrode interface, including water

$$2H_2O + 2e^- \rightleftharpoons 2OH^- + H_2. \tag{5}$$

Tappertzhofen et al.<sup>13</sup> propose another reduction reaction at the insulator/inert electrode interface, including oxygen and water:

$$^{1}/_{2}O_{2} + H_{2}O + 2e^{-} \rightarrow 2OH^{-}.$$
 (6)

These counterelectrode half-cell reactions are essential to sustain the redox reaction until Ni ions migrate through the insulating layer and reach the counter electrode for reduction. Once they do, Ni ions are reduced, and the processes of Ni and water reduction occur simultaneously at different reaction rates<sup>13</sup>. Therefore, the reactions involving water are crucial as initial counterpart reactions to maintain charge neutrality within the cell. It is important to note that the reaction Eq. (6) not only requires water but also oxygen. However, since reaction (5) only requires water, additional oxygen molecules present at the insulator/inert electrode interface will enhance the creation of counter charges, but are not necessary for the reaction. Thus, we focus on humidity as a crucial factor for the redox reaction. In a vacuum, there is less humidity. Thus, this water reduction reaction and,

consequently, the formation and filament growth are suppressed. Furthermore, the concentration of Ni ions is very limited due to the absence of charge compensation mechanisms<sup>25</sup>. It should be kept in mind that a relatively high ion mobility caused by the presence of water in ambient conditions can be an additional driving factor for the switching event<sup>13</sup>. In this case, the switching probability decreases in a vacuum because the ion mobility decreases due to a lack of moisture.

In the simulation (Fig. 4b), the effect of vacuum, i.e., less humidity, is considered with a lower Ni ion concentration c ( $10^{21}$  m<sup>-3</sup>, green) than that of the ambient atmosphere ( $c = 10^{24} \,\mathrm{m}^{-3}$ , orange). The higher one of the concentrations results from the fitting process. The lower concentration is chosen exemplarily to apply our theory in a qualitative way (see Supplementary Note 1 for details). The simulation results reveal that the switching time drastically increases with decreasing Ni ion concentration. Only very high voltages enable switching, and a long switching time  $t_{set}$  is needed. These simulations support our argument that a lack of water in the environment of our cells limits the formation of a Ni filament and can explain the suppressed forming of our cells in a vacuum (Fig. 3). Area-dependent measurements in ambient and vacuum conditions revealed a significant difference in the forming voltage for devices smaller than  $\sim 300 \, \mu \text{m}^2$ , but no difference in the forming voltage for larger devices (see Supplementary Fig. 3). We attribute this to residual water in the material stack still present in vacuum conditions: in large devices, sufficient water remains at the interfaces even under vacuum to enable the electrochemical reactions similar to those in ambient conditions. In contrast, in smaller devices, water in the material stack gets removed more efficiently. Thus, the absence of environmental moisture in a vacuum has a greater impact. Importantly, this indicates that the studied effect of ambient moisture on the formation may be more pronounced in nanoscale devices.

In summary, memristors based on multilayer h-BN sandwiched between Pd and Ni electrodes were investigated. The memristors exhibit repeatable bipolar resistive switching under voltage stress applied to the Ni electrode. Comparative electrical I-V measurements under ambient and vacuum conditions reveal the necessity of ambient air molecules for the resistive switching of the cells. The set kinetics of the memristors were investigated by switching the devices with voltage pulses ranging from minutes to nanoseconds. They can be described by the Butler-Volmer equation, which reflects the occurrence of redox reactions during resistive switching. Simulations confirm that the absence of humidity leads to drastically longer switching times and thus can explain the suppressed formation of our cells in a vacuum. These findings have important implications for potential applications of h-BN memristors, as computer chips in end-user applications are usually encapsulated to protect them from atmospheric influences. Further experiments are needed to analyze the exact dependency of the resistive switching performance on the relative humidity of the surrounding atmosphere. Knowing the amount of water needed for optimal resistive switching may allow adjusting the fabrication process accordingly. Additionally, detailed cyclic voltammetry measurements in different atmospheres can give insights into the exact electrochemical reactions at the interfaces. Furthermore, knowledge of the reaction equations may allow the material stack to be adapted so that resistive switching is still possible without water molecules.

#### Methods

#### **Device fabrication**

 $2~cm\times 2~cm$  silicon (Si) samples with 300 nm thermally oxidized silicon dioxide (SiO $_2$ ) were used as the starting substrates. The bottom electrodes (BEs) were defined via optical lithography, followed by 10 nm titanium (Ti) and 40 nm palladium (Pd) in situ deposition via electron beam evaporation. A subsequent lift-off process defined the contact areas. h-BN was grown via metalorganic chemical vapor deposition (MOCVD) on c-plane sapphire (with a 0.2° offcut toward the m-plane) in an AIXTRON Close Coupled Showerhead (CCS°) 2D R&D reactor in a  $19\times 2''$  configuration. A continuous h-BN film was formed via a one-step growth process at 1350 °C and 500 mbar pressure for 1600 s using borazine (B $_3$ N $_3$ H $_6$ ) as a precursor material and H $_2$  as a carrier gas. The film was subsequently transferred to the sample via a wet transfer approach. The top electrodes (TEs) were defined via a second optical lithography step, direct current (DC) sputtering of 30 nm nickel (Ni) and 30 nm aluminum (Al, in situ), and a subsequent lift-off process.

#### Structural device analysis

Optical microscope images were recorded with a Keyence laser scanning microscope VK-X3000. AFM measurements were done with a Bruker Dimension Icon AFM in tapping mode. Raman measurements were done with a WiTec Raman spectrometer alpha300R in mapping mode with an excitation laser wavelength of 532 nm with 15 mW laser power.

#### Electrical device analysis

Electrical measurements were performed in a cryogenic probe station "CRX-6.5 K" from LakeShore Cryotronics connected to a semiconductor parameter analyzer (SPA) "4200A-SCS" with two source measure unit (SMU) cards "Keithley 4200-SMU", each connected to a pre-amplifier "Keithley 4200-PA" from Tektronix. Additionally, a pulse measure unit (PMU) "4225-PMU" with two channels was installed, each connected to one remote pulse amplifier (RPM) "4225-RPM". The I-V measurements shown in Fig. 2 were performed with the SMUs. A fixed current measurement range of 100  $\mu$ A was used during the positive voltage sweeps. In contrast, an automatic current measurement range was used during the negative voltage sweeps due to the large difference in current magnitudes observed during reset events. The different choices for current measurement

ranges during the positive and negative voltage sweeps resulted in different sweep rates. The PMU was used for voltage pulse widths up to 10 ms, while set events occurring after several seconds were measured with the SMUs in constant biasing mode.

#### **Data availability**

The datasets generated and/or analyzed during this study are available from the corresponding author upon reasonable request.

#### **Abbreviations**

2D two-dimensional; h-BN hexagonal boron nitride; ECM electrochemical metallization;

Si silicon;
SiO<sub>2</sub> silicon dioxide;
BE bottom electrode;
Ti titanium;
Pd palladium;

MOCVD metalorganic chemical vapor deposition;

CCS® Close Coupled Showerhead;

B<sub>3</sub>N<sub>3</sub>H<sub>6</sub> borazine; TE top electrode; DC direct current; Ni nickel; Al aluminum;

AFM atomic force microscopy;
HRS high resistance state; *I-V* current-voltage;
LRS low resistance state

Received: 20 January 2025; Accepted: 29 April 2025;

Published online: 14 May 2025

#### References

- Lanza, M., Hui, F., Wen, C. & Ferrari, A. C. Resistive switching crossbar arrays based on layered materials. Adv. Mater. 35, 2205402 (2023).
- Li, M. et al. Imperfection-enabled memristive switching in van der Waals materials. Nat. Electron. 6, 491–505 (2023).
- Lemme, M. C., Akinwande, D., Huyghebaert, C. & Stampfer, C. 2D materials for future heterogeneous electronics. *Nat. Commun.* 13, 1392 (2022).
- Cassabois, G., Valvin, P. & Gil, B. Hexagonal boron nitride is an indirect bandgap semiconductor. *Nat. Photonics* 10, 262–266 (2016).
- Kim, J. et al. Attojoule hexagonal boron nitride-based memristor for highperformance neuromorphic computing. Small 20, 2403737 (2024).
- Teja Nibhanupudi, S. S. et al. Ultra-fast switching memristors based on two-dimensional materials. *Nat. Commun.* 15, 2334 (2024).
- Pan, C. et al. Coexistence of grain-boundaries-assisted bipolar and threshold resistive switching in multilayer hexagonal boron nitride. Adv. Funct. Mater. 27, 1604811 (2017).
- Völkel, L. et al. Resistive switching and current conduction mechanisms in hexagonal boron nitride threshold memristors with nickel electrodes. Adv. Funct. Mater. 34, 2300428 (2024).
- Zhuang, P. et al. Nonpolar resistive switching of multilayer-hBNbased memories. Adv. Electron. Mater. 6, 1900979 (2020).
- Villena, M. A. et al. Variability of metal/h-BN/metal memristors grown via chemical vapor deposition on different materials. *Microelectron. Reliab.* 102, 113410 (2019).
- Valov, I. Redox-based resistive switching memories (ReRAMs): electrochemical systems at the atomic scale. *ChemElectroChem* 1, 26–36 (2014).
- Milano, G. et al. Structure-dependent influence of moisture on resistive switching behavior of ZnO thin films. Adv. Mater. Interfaces 8, 2100915 (2021).

- Tappertzhofen, S. et al. Generic relevance of counter charges for cation-based nanoscale resistive switching memories. ACS Nano 7, 6396–6402 (2013).
- Valov, I. & Tsuruoka, T. Effects of moisture and redox reactions in VCM and ECM resistive switching memories. *J. Phys. Appl. Phys.* 51, 413001 (2018).
- Tsuruoka, T. et al. Humidity effects on the redox reactions and ionic transport in a Cu/Ta2O5 /Pt atomic switch structure. *Jpn. J. Appl. Phys.* 55, 06GJ09 (2016).
- Lübben, M., Wiefels, S., Waser, R. & Valov, I. Processes and effects of oxygen and moisture in resistively switching TaOx and HfOx. Adv. Electron. Mater. 4, 1700458 (2018).
- Wang, B. et al. Experimental observation and mitigation of dielectric screening in hexagonal boron nitride based resistive switching devices. Cryst. Res. Technol. 53, 1800006 (2018).
- Yang, F. et al. Effect of environmental contaminants on the interfacial properties of two-dimensional materials. Acc. Mater. Res. 3, 1022–1032 (2022).
- Smith, A. D. et al. Resistive graphene humidity sensors with rapid and direct electrical readout. *Nanoscale* 7, 19099–19109 (2015).
- Fan, X. et al. Humidity and CO2 gas sensing properties of double-layer graphene. Carbon 127, 576–587 (2018).
- Ahmad, R. W. et al. Variability-aware modelling of electrochemical metallization memory cells. *Neuromorphic Comput. Eng.* https://doi. org/10.1088/2634-4386/ad57e7 (2024).
- Menzel, S., Tappertzhofen, S., Waser, R. & Valov, I. Switching kinetics of electrochemical metallization memory cells. *Phys. Chem. Chem. Phys.* 15, 6945 (2013).
- 23. Gorbachev, R. V. et al. Hunting for monolayer boron nitride: optical and Raman signatures. Small 7, 465–468 (2011).
- Ielmini, D., Waser, R. & Akinaga, H. Resistive Switching: From Fundamentals of Nanoionic Redox Processes to Memristive Device Applications (Wiley-VCH, 2016).
- Lübben, M. et al. SET kinetics of electrochemical metallization cells: influence of counter-electrodes in SiO<sub>2</sub>/Ag based systems. Nanotechnology 28, 135205 (2017).
- Chekol, S. A., Menzel, S., Ahmad, R. W., Waser, R. & Hoffmann-Eifert, S. Effect of the threshold kinetics on the filament relaxation behavior of Ag-based diffusive memristors. Adv. Funct. Mater. 32, 2111242 (2022).
- Butler, J. A. V. Studies in heterogeneous equilibria. Part I. Conditions at the boundary surface of crystalline solids and liquids and the application of statistical mechanics. *Trans. Faraday Soc.* 19, 659 (1924).
- 28. Dickinson, E. J. F. & Wain, A. J. The Butler-Volmer equation in electrochemical theory: origins, value, and practical application. *J. Electroanal. Chem.* **872**, 114145 (2020).
- 29. Mott, M. F. & Gurney, R. W. Electronic Processes in Ionic Crystals (Dover: UK, 1948).

#### Acknowledgements

We gratefully acknowledge financial support from the German Federal Ministry of Education and Research (BMBF) within the projects NEUROTEC 2 (16ME0399, 16ME0398K, 16ME0400) and NeuroSys (03ZU1106AA, 03ZU1106BA), and from Deutsche Forschungsgemeinschaft (DFG) within the project SPP2262 MEMMEA, project no. 441918103 (MemrisTec). We

acknowledge funding from the European Union's Horizon Europe research and innovation program (via CHIPS-JU) under the project ENERGIZE (101194458). The views and opinions expressed are those of the authors only and do not necessarily reflect those of the European Union or the European Commission. Neither the European Union nor the European Commission can be held responsible for them.

#### **Author contributions**

The experiments were conceived by L.V., R.W.A., S.M., M.H., and M.C.L. The fabrication of the samples was carried out by L.V. h-BN was synthesized by S.K. and S.P. The electrical measurements were performed by L.V. Raman spectra and AFM images were obtained by L.V. The simulations were conducted by R.W.A., A.B., and S.M. The data were analyzed by L.V., D.B., S.C., J.L., R.W.A., A.B., S.M., and M.C.L. All authors collaborated on the interpretation of the experiments. The manuscript was written and revised by all. The work was supervised by S.M. and M.C.L.

#### **Funding**

Open Access funding enabled and organized by Projekt DEAL.

#### **Competing interests**

M.C.L. is the managing director of the non-profit company AMO GmbH, whereas S.P., S.K., and M.H. are employees of AIXTRON SE. Both companies are partners of several publicly funded research projects and are working on the growth and device integration of 2D materials. L.V., R.W.A., A.B., D.B., S.C., J.L., and S.M. have no competing interests.

#### **Additional information**

**Supplementary information** The online version contains supplementary material available at https://doi.org/10.1038/s41699-025-00566-0.

**Correspondence** and requests for materials should be addressed to Max C. Lemme.

Reprints and permissions information is available at http://www.nature.com/reprints

**Publisher's note** Springer Nature remains neutral with regard to jurisdictional claims in published maps and institutional affiliations.

Open Access This article is licensed under a Creative Commons Attribution 4.0 International License, which permits use, sharing, adaptation, distribution and reproduction in any medium or format, as long as you give appropriate credit to the original author(s) and the source, provide a link to the Creative Commons licence, and indicate if changes were made. The images or other third party material in this article are included in the article's Creative Commons licence, unless indicated otherwise in a credit line to the material. If material is not included in the article's Creative Commons licence and your intended use is not permitted by statutory regulation or exceeds the permitted use, you will need to obtain permission directly from the copyright holder. To view a copy of this licence, visit http://creativecommons.org/licenses/by/4.0/.

© The Author(s) 2025